Research Article Vol. 12, No. 11 / 1 Nov 2021 / Biomedical Optics Express 7009
Biomedical Optics EXPRESS

Label-free imaging of age-related cardiac structural changes in non-human primates using multiphoton nonlinear microscopy

AMARA KHAN,[1,2] FERNANDA RAMOS-GOMES,[1] ANDREA MARKUS,[1] MATTHIAS MIETSCH,[2,3] RABEA HINKEL,[2,3,4] AND FRAUKE ALVES[1,2,5,6,*]

[1]*Max-Planck-Institute for Experimental Medicine, Translational Molecular Imaging, Göttingen, Germany*
[2]*DZHK (German Center for Cardiovascular Research), Partner site Göttingen, 37077 Göttingen, Germany*
[3]*Laboratory Animal Science Unit, German Primate Center, Leibniz Institute for Primate Research, Göttingen, Germany*
[4]*Stiftung Tierärztliche Hochschule Hannover, Hannover, Germany*
[5]*University Medical Center Göttingen, Institute for Diagnostic and Interventional Radiology & Clinic for Hematology and Medical Oncology, Göttingen, Germany*
[6]*Cluster of Excellence "Multiscale Bioimaging: from Molecular Machines to Networks of Excitable Cells," Göttingen, Germany*
[*]*falves@gwdg.de*

Abstract: Heart failure is one of the most common causes of morbidity and mortality. Both maturational abnormalities and age-associated cardiac pathologies contribute to heart failure. Imaging-based assessment to discern detailed cardiac structure at various maturational stages is imperative for understanding mechanisms behind cardiac growth and aging. Using multiphoton nonlinear optical microscopy (NLOM) based label-free imaging, we investigated cardiac structural composition in a human-relevant aging model, the common marmoset monkey (*Callithrix jacchus*). Animals were divided into three different age groups including neonatal, young adult and old. By devising a unique strategy for segregating collagen and myosin emitted second harmonic generation (SHG) signals, we performed a volumetric assessment of collagen and total scattering tissue (collagen + myosin). Aged marmoset hearts exhibited an increase in collagen and total scattering tissue volume at the sites of severe tissue remodelling indicating age-related cardiac fibrosis. Significantly low scattering tissue volume in neonatal marmoset hearts was attributed to a lack of binding between the myofibrils in maturing cardiac tissue. Comprehensive quantitative assessment of structural composition during maturation and aging of marmoset hearts revealed significant differences in myofibril length, alignment, curvature and angular distribution. In conclusion, label-free high-resolution NLOM facilitates visualization and quantification of subcellular structural features for understanding vital age-related morphological alterations in the marmoset heart.

1. Introduction

Cardiac maturation and growth are dynamic processes that involve complex and well-orchestrated biochemical, physiological, and anatomical changes that define cardiac function in different age groups. Our current understanding of postnatal cardiac development and aging is limited by an overall lack of reliable data about the cardiomyocyte (CM) growth and proliferation mechanisms in the heart from birth to early adulthood and old age [1–4].

Fundamental differences in cardiac structure and physiology exist between a neonatal and adult mammalian heart in several ways, mainly because the neonatal CMs are not fully developed. Structural maturity and myocardial growth in humans are based on CM enlargement and

#432102 https://doi.org/10.1364/BOE.432102
Journal © 2021 Received 25 May 2021; revised 26 Aug 2021; accepted 26 Aug 2021; published 19 Oct 2021

Biomedical Optics EXPRESS

proliferation at the early postnatal developmental stages [2,5–7]. Shortly after birth, numerous transitions are triggered in the neonatal heart that initiate complex remodeling from a fetal state into an adult heart. Radiocarbon birth dating has further shown that a small portion of CMs is replaced in humans older than 20 years [8]. Imaging-based assessment to discern detailed cardiac structural composition in neonatal hearts and its comparison at the cellular level with an adult heart and aged hearts is so far greatly lacking.

Over the span of cardiac growth and structural maturation, an aged heart begins to display pathophysiological remodeling which also makes aging one of the leading risk factors for heart failure related morbidity and mortality. Aged heart exhibits the development of left ventricular (LV) hypertrophy, excessive extracellular matrix (ECM) deposition and CM senescence even in absence of underlying pathology [9–14]. Evolving evidence shows that inflammatory and fibrogenic pathways play a pivotal role in triggering CM as well as vascular aging [13,15,16]. Besides tissue remodeling, a myriad of additional cellular factors is associated with cardiac aging including age-related apoptosis and excitation-contraction coupling (ECC) disorder due to impaired Calcium (Ca^{2+}) handling [12,17].

Elucidating myocardial structure is imperative for investigating cardiac growth, maturation and age-related pathophysiological remodeling. Imaging cardiac aging in non-human primates (NHPs) can provide highly clinically relevant data, as they reflect a comparable life span as humans. Unlike other laboratory species such as rodents or even large animal models (pigs or sheep), NHPs demonstrate similar aging characteristics and pathophysiology as humans [18]. Furthermore, reports on the influence of cardiac maturation and aging in NHPs is largely lacking [3,14]. Among NHPs, using the common marmoset monkeys (*Callithrix jacchus*) model in aging research provides various advantages such as relatively small body size and short generation time [14].

Histological examination is a gold-standard for morphological assessment of the heart, but it lacks adequate resolution and specificity. Alternatively, high-resolution microscopy techniques offer detailed visualization on the cellular and sub-cellular level such as confocal microscopy and super-resolution microscopy techniques [19]. However, these techniques require labor intensive sample preparation and labeling of target proteins using fluorescent labeled antibodies or dyes which might lead to unspecific binding and excess labelling if not performed carefully [20]. Furthermore, photobleaching of the fluorophore can hinder repetitive imaging and quantitative analysis [21]. Multiphoton nonlinear optical microscopy (NLOM) provides a promising alternative as it can image intrinsic signals emitted in the form of two-photon excitation fluorescence (TPEF) and second harmonic generation (SHG). Since in NLOM an endogenous fluorescent molecule with specific physical properties and order is excited by pulsed near infra-red (IR) laser and the emitted signal is detected at ultrasensitive detectors, this allows increased imaging depth, high specificity, and reproducibility [22,23].

Unlike TPEF, in which two photons are absorbed by the target structure to produce a fluorescent signal as a single photon with some loss of energy, SHG does not involve photon absorption and energy decimation. Instead, SHG as a nonlinear coherent scattering process results in phase matching and summation of light waves and involves the conversion of two excitation photons into a single emission photon with twice the energy and thus, half of the excitation wavelength. Biological materials with repetitive non-centrosymmetric units, including myosin within the striated muscle and fibrillar collagen which are both integral components of cardiac structure, facilitate the emission of SHG [23,24].

The intensity of SHG from myosin (striated muscle) and collagen is crucially dependent on i) the organization and size of these signal-eliciting structures, ii) the excitation/detection approach and iii) the power and polarization of the incident light [23–26]. We recently established an SHG imaging approach for label-free and high-resolution visualization of cardiac remodeling and fibrosis progression at different stages in a cardiac pressure-overload mouse model. In our

Biomedical Optics EXPRESS

previous work, the SHG emission from collagen and myosin was segregated based on structural morphology and was performed in two-dimensions (2D) only [27].

In the present study, detailed analysis of subcellular structural components during maturation and aging was performed in three-dimensional images (3D) using NLOM label-free imaging in common marmosets belonging to three different age groups including neonatal, young adult and old geriatric without any additional disease or comorbidities. To achieve this, we harnessed the differences between collagen and myosin emitted SHG and devised a sophisticated label-free imaging strategy to enable signal segregation from the two harmonophores. This resulted in the reliable volumetric assessment of connective tissue and total scattering tissue (myosin + collagen) demonstrating cardiac fibrosis in old marmosets and differences in morphological features of myofibrils in all age groups.

2. Materials and methods

2.1. Animal groups and organ collection

Experiments were conducted on nine common marmoset monkeys (*Callithrix jacchus*) with an age ranging from 6 days to 13 years (Table S1). The study cohort consisted of 1 female neonatal marmoset and 8 males (Table S1). The animals were divided into three groups – neonatal (<4 weeks, n = 3), young adult (1–4 years, n = 3), and old (>10 years, n = 3) following general classifications according to the literature [28].

All animals were raised and kept in accordance with the German Animal Welfare Act. All animal procedures were performed in compliance with the guidelines of the European Directive (2010/63/ EU) and the German ethical laws. Animals used in this study were either euthanized due to animal welfare reasons (corresponding to humane endpoints) or they were euthanized for organ removal for other scientific purposes (according to §4 TierSchG).

To sacrifice, animals were deeply anaesthetized with either ketamine (intramuscular >15mg/kg, Ketamin 10%, WDT) or a combination of alphaxalone (i.m. 10mg/kg, Alfaxan 10mg/ml, Jurox) and diazepam (0.125mg/animal, Diazepam-ratiopharm 5mg/ml, ratiopharm GmbH) followed by an intraperitoneal or intravenous administration of pentobarbital (>150mg/kg). Hearts were collected in addition to a broad spectrum of organs.

2.2. Sample preparation

Freshly explanted hearts were briefly washed in phosphate buffered saline (PBS) and then fixed in 4% formaldehyde solution (FA) overnight at room temperature (RT). Hearts were cut into transverse tissue sections for SHG imaging and adjacent tissue sections from the same heart sample were used for histology. Briefly, for sectioning, hearts were embedded in 5% agarose and were cut into 50 µm, 100 µm and 1 mm sections using a vibratome (VT1000 S; Leica Biosystems). The 50 and 100 µm thick tissue sections were used for NLOM and were stored in PBS containing 0.04% sodium azide. The 1 mm sections were embedded in paraffin for histology (Fig. S1).

2.3. Multiphoton nonlinear optical microscopy

Label-free SHG and TPEF imaging were performed on an upright TriM Scope II multiphoton microscope (Miltenyi Biotec) equipped with a tunable Ti:sapphire laser (Ti:Sa, 670–980 nm; Cronus, Miltenyi Biotec). Images were acquired using a Zeiss W Plan-Apochromat 20x (NA 1.0) water immersion objective. The signals were detected at 3 detectors with differential filter configuration (434/20, 434/20 and 525/50 long pass, Semrock). Cardiac tissue sections were excited at 870 nm with an estimated maximum power of 100–150 mW. It was calculated as the percentage of the total output power i.e.,12.5-15% of ~900-1000 mW total laser power. The percentage of illumination power was set at the ImSpector software (LaVision BioTec) based on the overall signal intensity, laser alignment and stability on the day of imaging. Simultaneous

Biomedical Optics EXPRESS

backscattered SHG and autofluorescence signals were split by a 495 nm and T560 nm long pass dichroic mirror (Semrock) and detected through the objective lens at PMT detectors (Hamamatsu) and forward SHG signal was collected using a 1.4 NA condenser lens at a third PMT detector (Hamamatsu).

Since polarisation resolved SHG imaging was not performed, collagen fibrils of varying orientation which are sensitive to polarization could be fully retrieved as backscattered SHG in our imaging approach.

For the overview images, an image size of 336 × 336 µm with 1024 × 1024 pixels and a pixel dwell time of 2.19 µs was used. Magnified images at the ROI were acquired using 112 × 112 µm image size, 1024 × 1024 pixels or 512 × 512 pixels to achieve adequate image resolution for analysis. In total, 15 high resolution image volumes (x = 2; y = 2; z = 50) at randomly assigned ROIs were acquired for each sample (45 image volumes per group). The ROIs were selected within the myocardial layer of the left ventricular (LV) and interventricular septum (IVS) wall (Fig. S2).

2.4. Histology

The paraffin-embedded 1 mm cardiac tissue slices from regions adjacent to tissue sections used for NLOM imaging were cut into 2 µm sections. The sections were deparaffinized and dehydrated followed by haematoxylin & eosin (H&E) and Masson's Trichrome staining (MTS), performed as described before [27].

The images were acquired with an Axiovert 200 M inverted microscope (Carl Zeiss Microscopy GmbH). Image generation and processing were performed with the software AxioVision Rel.4.6 (https://carl-zeissaxiov isionrel.software.informer.com/4.6/) and Fiji, respectively.

2.5. Image processing and statistical analysis

2D micrographs were processed with Fiji for assessing the histogram, intensity and length of the myofibrils. Myofibril curvature and alignment were quantified using the TWOMBLI plugin in ImageJ [29]. 3D volumes, surface rendering of myofibril segments and angular distribution were processed and analysed using Imaris 9.6.0 (Bitplane) and Graph Pad Prism 9 (Graph Pad Software, Inc.). For statistical analysis, the t-test for the same mean implemented in Graph Pad Prism 9 was used with a p-value of 0.05 (*) as a margin for statistical significance. Graphs were prepared using Graph Pad Prism 9 and Microsoft Excel (© Microsoft Corporation, 2021).

3. Results

3.1. Label-free imaging by NLOM for distinction of myosin and collagen

The most common application of NLOM involves excitation of exogenous or endogenous fluorescent molecules i.e., TPEF. For establishing a label-free imaging approach in marmoset cardiac tissue, we applied TPEF to detect only endogenous fluorescence signals emitted from intrinsic molecules in unstained tissue slices enabling repetitive and long-term imaging of the samples. Extracellular fluorescence in cardiac tissue originated from blood cells, elastin and also collagen but only with negligible intensity (Fig. 1,) whereas the majority of intracellular fluorescence arises from the mitochondrial proteins nicotinamide adenine dinucleotide (NADH), flavin adenine dinucleotide (FAD) and other fluorescence emitting proteins. Nuclei, on the other hand, lacked a fluorescent signal and hence appeared dark, and were detected easily due to their elongated morphology in the myocardium (Fig. 1,).

Specimens amenable to bidirectional (forward and backward) detection include thin tissue slices or cleared tissue samples possessing high optical transparency while thick and highly opaque specimens are detected as backward scatter only. Since 50 µm cardiac tissue slices, which were relatively transparent, were used for NLOM imaging, the SH emission signals were

Biomedical Optics EXPRESS

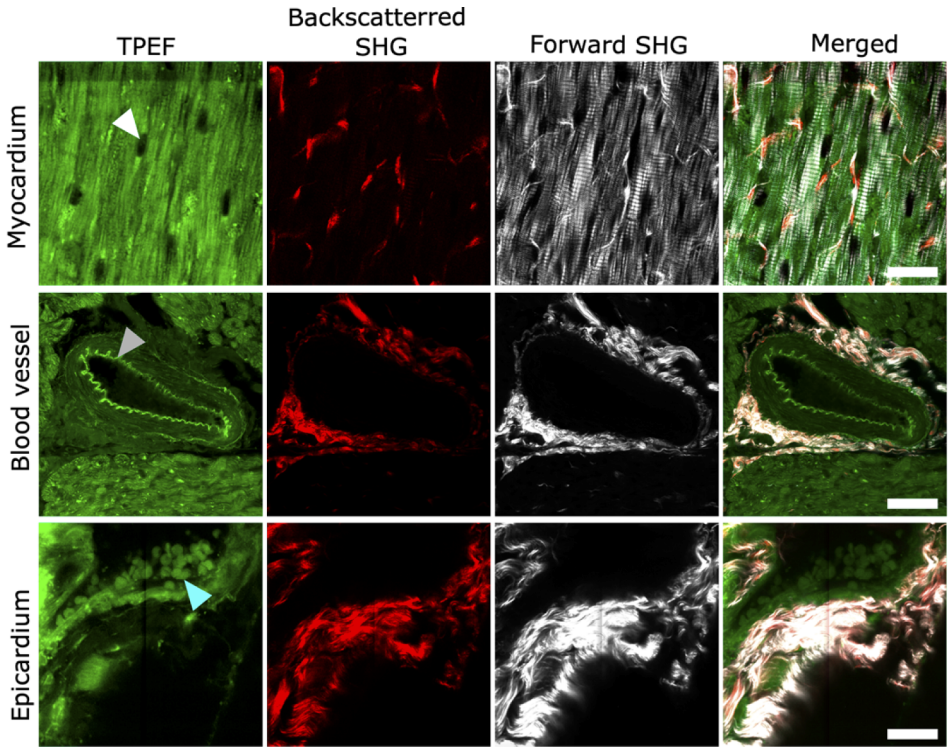

Fig. 1. Label-free NLOM images of old marmoset cardiac tissue. Representative TPEF, backscattered SHG, forward propagating SHG and merged images are shown for coronary blood vessel, myocardium and epicardial wall from the same heart. TPEF arises from endogenous fluorophores such as blood cells (marked by cyan arrowhead), elastin (marked by grey arrowhead) and other intracellular fluorescent proteins, while the nuclei appear dark (marked by white arrowhead). Backscattered SHG emission is detected mainly from collagen while the forward propagating SHG emission originates with high intensity from both collagen and myosin at the epicardium and myocardium and around the blood vessel. Merged images show signal emission from all channels. Scale bar: 25 µm in all images.

collected in both backscattered (epi-) and forward propagating direction (Fig. 1). SHG being a nonlinear coherent process is strongly influenced by the harmonophores' spacing, concentration and orientation hence these aspects were taken into account to enable segregation of SH emission from myosin and collagen. In our experimental design, collagen emitted SHG was detected in epi-direction while at the forward detector combined SH signals from myosin and collagen were visualized (Fig. 1 and 2).

Figure 2 exhibits the detailed comparison of SHG emission from the two harmonophores in adult cardiac tissue detected in both forward and backscattered directions. All images shown in Fig. 2 were acquired at the same regions simultaneously in both directions using the same illumination power, excitation (870 nm) and emission wavelengths (434 ± 20 nm) (Fig. 2). It is evident that in general the forward signals are stronger than the ones detected in the backward direction. Backward myosin SHG (mean intensity = 165.0) was considerably weaker than forward myosin SHG signal with a poor signal-to-noise ratio (Fig. 2(a) and (b)). Contrarily, the backscattered collagen signal had optimum signal intensity (mean intensity = 1279.8), while it caused intense signal saturation at the forward detector (mean intensity = 6857.5) when acquired with identical image acquisition settings used for imaging myosin (Fig. 2(c) and (d)).

Biomedical Optics EXPRESS

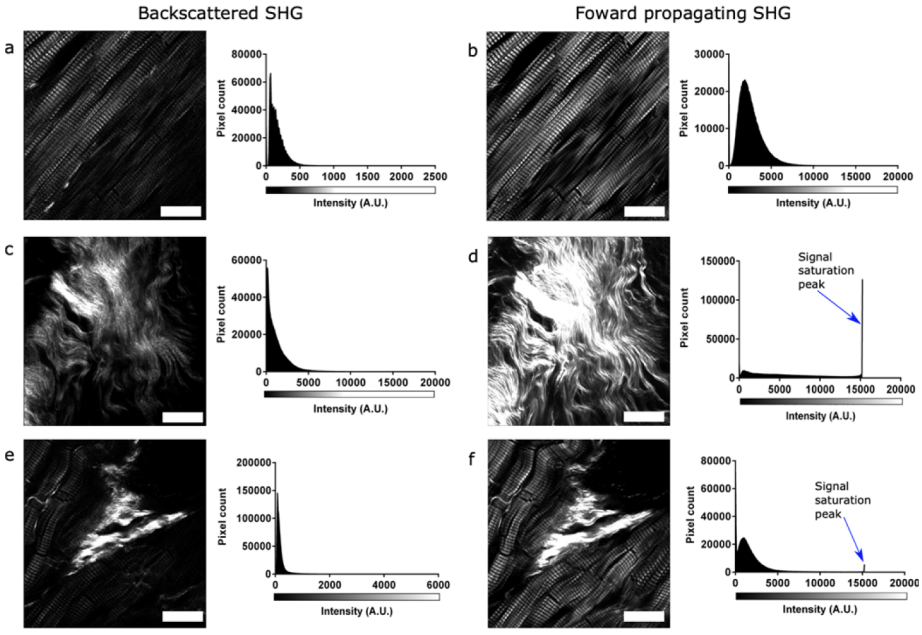

Fig. 2. Comparison of forward and backscattered SHG signal in adult marmoset cardiac tissue. Representative SHG images are shown for the same regions for backscattered (epi-) (left panel) and forward (right panel) detection with their respective histograms. Images and histograms are shown for SHG from different structures including (a-b) myosin (excitation power 120 mW) (c-d) collagen (excitation power 120 mW) and (e-f) both myosin and collagen (excitation power 120 mW). Scale bar: 25 µm in all images. All histograms are presented in a 16-bit image format.

The differences in the forward/backward SHG intensity ratios mainly arise from the structural assembly of the harmonophores since the image acquisition settings for forward and backward SHG signal generation and detection were identical (Fig. 2). For quantification purposes, SHG signal in the forward channel from both harmonophores (mean intensity = 2572) was used for determining total scattering tissue volume while the signal intensities from collagen were ideal for quantification in the backscattered direction (Fig. 2(e) and (f)). The discrepancy in the amount of collagen detection at the backscattered and forward detector was minimized by using thin tissue slices of 50 µm for the quantification of collagen.

3.2. Volumetric quantification of age-related differences in collagen and total scattering tissue content

To investigate the overall tissue structural composition of collagen and myosin in different age groups, label-free imaging was performed on cardiac tissue sections obtained from neonatal (n = 3), young adult (n = 3) and old (n = 3) marmosets (Fig. S3 and Visualization 1, Visualization 2, Visualization 3). Neonatal hearts were compared to adult hearts for assessing cardiac maturation and growth. The age-associated cardiac remodeling was examined in old hearts. 3D micrographs for volumetric assessment in 50 µm tissue sections were acquired at 45 randomly selected regions of interest (ROIs) per group at the myocardium of the LV and the IVS wall for all three maturation stages (Fig. 3(a) and Fig. S2). The backscattered signal exhibited SHG exclusively emitted from collagen while the forward SH signal was generated from both myosin and collagen (referred to as the total scattering tissue volume) (Fig. 3(a)). The collagen tissue volume increased significantly with age wherein the neonatal hearts had the lowest collagen volume (p-value = 0.0005) followed

Biomedical Optics EXPRESS

by adult hearts (p-value = 0.0184) and old hearts revealed the highest collagen volume (Fig. 3(b)). The data for average raw volumes of collagen and total scattering tissue volume showed an overall increase in tissue content with aging (Fig. 3(c), See Visualization 1, Visualization 2 and Visualization 3). Compared to the neonatal hearts, the adult and old hearts had significantly higher total scattering tissue volume at the ROIs (p-value = 0.0001).

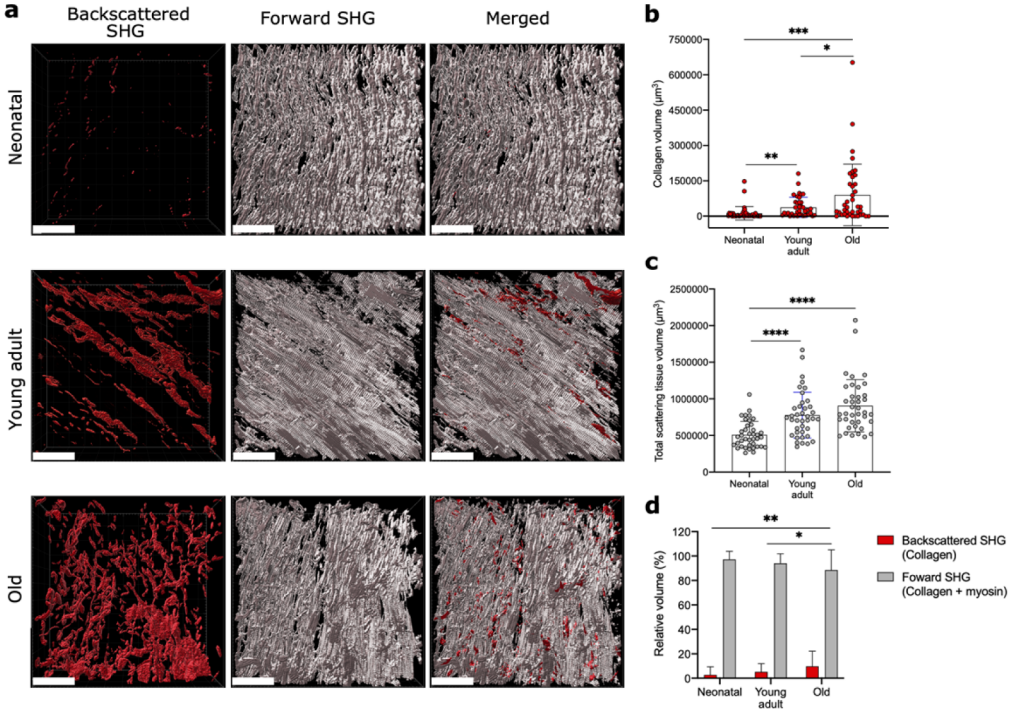

Fig. 3. Quantification of collagen and myosin content at different cardiac developmental stages. a) 3D rendering of backscattered SHG emission from collagen, forward SHG emission from both myosin and collagen (total scattering tissue volume) and merged images are shown for neonatal, young adult and old marmoset cardiac tissue. b-c) Graphs showing volume (μm^3) of backscattered SHG (collagen) and forward SHG (total scattering tissue volume). d) Percentage of relative tissue volumes detected at the backscattered and forward channels. Scale bars: 50 µm in all images. All images were acquired in the range of 120–125 mW.

Further, the percentage backscattered (collagen) and forward SHG (total scattering tissue) volumes were compared to assess the relative tissue composition. The percentage for backscattered SH signal was determined from the total scattering tissue volume (forward/backward SHG) while for forward SHG the percentage difference (forward − backscattered/forward) was calculated. The neonatal heart had an overall lowest total scattering tissue volume and was mainly composed of muscle (Fig. 3(b) - (d)). The connective tissue (collagen) in the neonatal heart was found to be less than 3% of total scattering tissue (Fig. 3(d); Visualization 1 and Visualization 3). Moreover, in contrast to the adult hearts (collagen volume ~ 5%), the old hearts also had a significantly higher volume of connective tissue (~ 12%) indicating the development of interstitial fibrosis causing an overall disruption of the surrounding muscle mass (Fig. 3(a) and (d); Visualization 2 and Visualization 3). Interestingly, the relative total scattering tissue volume was significantly lower (~ 88%) than in adults (~ 95%) and neonatal (> 98%) hearts (Fig. 3(c)), revealing a high collagen-based tissue composition in the old hearts (Visualization 3).

Biomedical Optics EXPRESS

3.3. Comprehensive analysis of age-related morphological changes in myofibrils

To further investigate the effects of tissue growth and maturation, the impact of the excess collagen deposition and tissue volume on the muscle structure, more than 50 2D micrographs were analyzed per group for examining the structure and spacing of myofibrils at the cellular level in the three age groups of marmosets. In the old hearts, the myocardium appeared compact with undulated myofibrils revealing a hypercontractile state (Fig. 4(a)). The muscle mass in adult hearts, similar to old hearts, was also dense with lower spacing between myofibrils, however, these were not hypercontracted (Fig. 4(a)). In comparison, the neonatal hearts displayed the highest degree of spacing between myofibrils which lacked overall organization and binding (Fig. 4(a)). The intercalated disks (ICDs) that bind the myofibrils were not visible in the neonatal hearts indicating that these were not fully developed in the cardiac tissue at this stage (Fig. 4(a)).

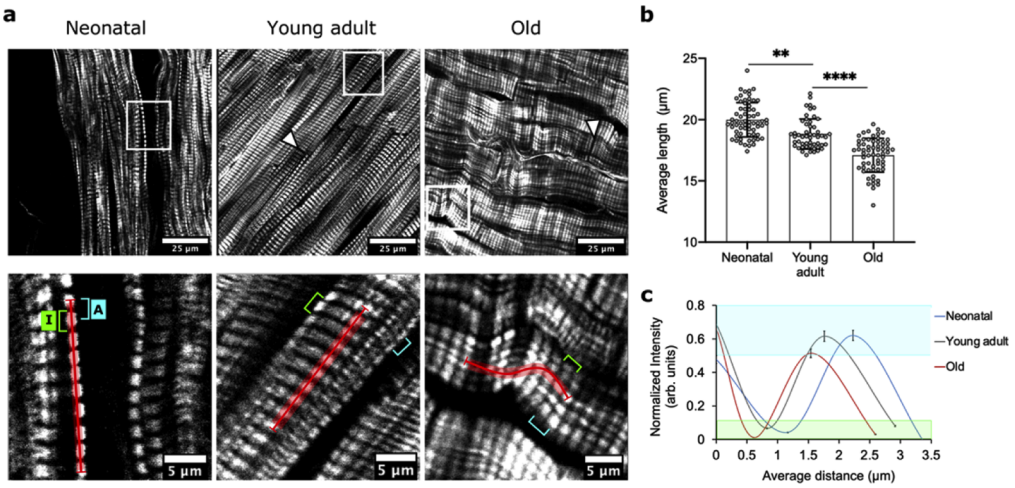

Fig. 4. Myofibril morphology at different cardiac maturation stages. a) Representative images of NLOM showing the arrangement of myosin fibers in neonatal (n = 3), adult (n = 3) and old (n = 3) marmoset hearts with overview images (top) and magnified images at the ROI marked by the white box (bottom). The white arrowheads mark the intercalated disks which were not visible in neonatal hearts. b) Graph for the average length of myofibril segment along the profile (marked by the red line in zoomed-in images). c) Normalized intensity and average spacing are shown for the distance between two SHG emitting anisotropic A-bands (cyan in a) and two non-SHG emitting isotropic I-bands (green in a); the distance profiles for A-bands lie within the shaded cyan box and for I-band within the green shaded box, respectively. Scale bars: 25 µm in overview images (top panel) and 5 µm in magnified ROI images (bottom panel); the whiskers in c show 5% error margin.

The differences in spacing of myofibrils were quantified in zoomed-in images along ten SHG emitting myosin packed anisotropic (A) bands and nine non-SHG emitting isotropic (I) bands containing actin filaments (Fig. 4(a), bottom). This micro-assessment of myofibrils for determining length was only possible on segments of myofibrils because ICDs could not be identified in immature neonatal hearts, and the mature myocardium of adult and old hearts comprised of overlapping myofibrils. The average length of these myofibril segments calculated along the ten A-bands was highest in neonatal hearts (20.0 ± 1.40 µm), reflecting an overall high-level of spacing which reduced significantly with cardiac tissue maturity in adult hearts (18.9 ± 1.27 µm, p-value = 0.0002) (Fig. 4(b)). In old hearts, the length of the hypercontracted myofibrils was found to be significantly lower (17.1 ± 1.3 µm) as compared to adult and neonatal hearts (p-value = 0.0001) (Fig. 4(b)). This significantly reduced spacing in hypercontracted

Biomedical Optics EXPRESS

myofibrils which might also contribute to the high tissue volume in these hearts (Fig. 3(b)). Upon closer inspection, it was further revealed that the distance between two isolated A-bands and I-bands also followed a similar pattern (Fig. 4(a) and (c)). This is demonstrated by the oscillation curve in Fig. 3(c) which was produced by measuring signal intensity of A- and I-bands and by calculating the average distance between these points along ten A-bands and nine I-bands. Out of these, normalized intensity and average distance are shown for the first two A-bands and I-bands for a clear graphical representation. The values for intensity and distance were obtained using ImageJ software and the curve was prepared in Microsoft excel (Fig. 4(c)). These results displayed the highest A-band to A-band distance in neonatal hearts (2.22 ± 0.09 µm), followed by adult hearts (1.76 ± 0.20 µm) and the lowest distance was observed in the old hearts (1.54 ± 0.02 µm) (Fig.4c). Similarly, the distance between two subsequent I-bands in neonatal tissues was highest (2.19 ± 0.06 µm) which was reduced in adult hearts (2.10 ± 0.21 µm) and old hearts (1.99 ± 0.17 µm) (Fig. 4(c)). These distinct distance profiles in all age groups thus present varying degrees of tissue maturation at the structural level.

Since myofibril assembly and arrangement presented diverse patterns in all three age groups, further assessment of myofibril morphology was performed on entire 2D micrographs obtained at random ROIs. Briefly, by using the TWOMBLI [29] (The Workflow Of Matrix BioLogy Informatics) plugin in Fiji, the spatial metrics for each group were derived and applied to the Ridge Detection tool for optimal masking of the images (Fig. 5(a)). Following the mask generation, the patterning of myofibrils was defined by two metrics – alignment and curvature. The alignment parameter captured the extent of myofibril orientation in a similar direction within the field of view where a high value (close to 1) presents perfect alignment while a lower value (close to 0) presents isotropy. Our results demonstrated significant differences in myofibril alignment in neonatal (p-value = 0.0001) and old hearts (p-value = 0.0001) as compared to young adult hearts (Fig. 5(b)). The disassembly of neonatal myofibrils is attributed to the lack of binding, further supporting the observation that ICDs are not fully developed at this maturational stage (Fig. 4(a)). The significantly low alignment in old hearts suggests structural disruption that may occur due to excessive ECM deposition.

The curvature metric measures the average change in angle moving incrementally along the masked region. The adult hearts displayed a high-level of straightness while the neonatal and old hearts revealed varying curvatures in the myofibril assembly. In neonatal hearts, the large range of curvature indicated an overall loose structure with undefined symmetry which was significantly different from the old hearts (p-value = 0.0091). The old hearts also displayed a significantly different curvature as compared to the adult hearts (p-value = 0.0013) (Fig. 5(c)). The tight curve radius in the old hearts further substantiates the presence of hypercontractile myofibrils.

Micro-level 3D evaluation was performed as a proof-of-concept to evaluate the differences in myofibril morphology and assembly in neonatal, young adult and old hearts from the high-resolution image volumes. Eight fragments of myofibrils per group were cropped in 3D from the entire tissue volume selectively to depict the distinct structural features attributed to the age group, i.e. disarrayed myofibrils were selected in neonatal hearts and hypercontracted myofibrils were chosen in old hearts to reflect altered angular distribution in these age groups. These 3D myofibril fragments contained ten A and nine I-bands (Fig. S4). 3D surface rendering of the isolated myofibril segments enabled marking measurement points at the center of the object i.e., at the individual A-band (Fig. S3 and Fig. 6(a)). The angle between each measurement point exhibited the angular distribution at the micro-level. The adult heart presented the highest degree of straightness with an average angle of 177 ± 2.0 Â° which was significantly altered in neonatal hearts (p-value = 0.0108) with an average angle of 171 ± 3.7 Â° (Fig. 6(b)). The highest range of angular distribution was observed in the hypercontracted myofibrils of the old hearts with an average angle of 156 ± 16.6 Â° (p-value = 0.0256) (Fig. 6(b)). The changes in

Biomedical Optics EXPRESS

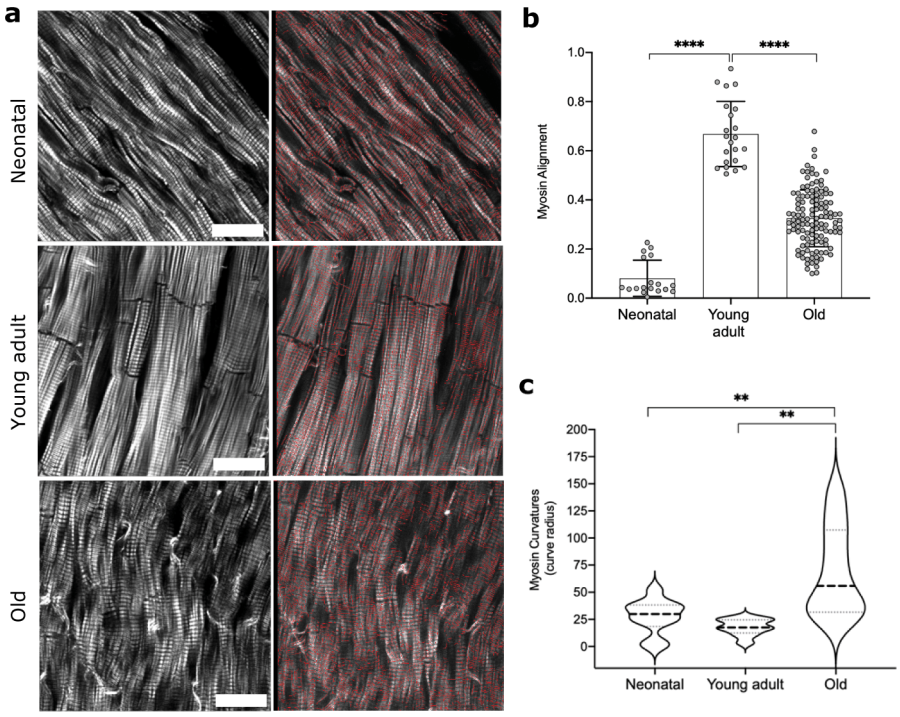

Fig. 5. Assessment of myofibril organization in the myocardium. a) Representative NLOM 2D micrographs (left panel) and respective masked images (right panel) showing myofibril organization in neonatal, young adult and old hearts. b-c) Graphs showing average myofibril alignment and myofibril curvature in all age groups. Scale bar: 25 µm for all images.

angular distribution reflect the overall structural integrity and organization at the micro-level in the different age groups of the marmoset model.

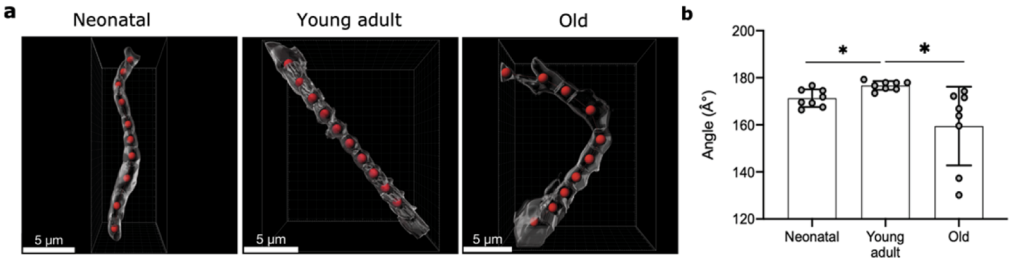

Fig. 6. 3D assessment of angular distribution in the isolated myofibril segments. (a) Segments of myofibrils containing 10 A-bands are shown for neonatal, young adult and old hearts marked with measurement points in red. (b) Graph showing the angular distribution between the measurement points for all age groups. Scale bar: 5 µm for all images.

3.4. Validation of structural differences in all age groups

The TPEF generated autofluorescence signal and histology of the myocardium further validated the differences in overall tissue composition of the three age groups. A striking difference was the cellularity of the neonatal myocardium. The neonatal myocardial cells are generally smaller than the adult CMs and thus displayed a higher nuclear to cytoplasm ratio (Fig. 7).

Biomedical Optics EXPRESS

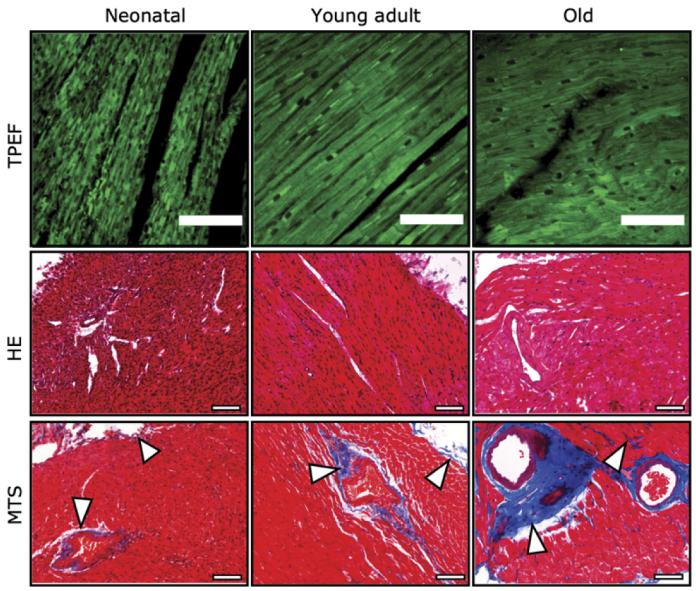

Fig. 7. Comparison of neonatal, young adult and old myocardium morphology. TPEF emitted autofluorescence in vibratome sections and Haematoxylin & Eosin (HE) staining in paraffin sections show the overall morphology of the myocardium and the nuclear to cytoplasm ratio. Masson-trichrome stained (MTS) tissue sections present the collagen deposition in blue (shown by white arrowheads) and muscle in red. Scale bar: 100 µm in all images.

Excess collagen deposition was found in the old marmoset, while in neonatal and adult animals, collagen was mainly present at the epicardial wall and the vicinity of blood vessels (Fig. 7, bottom row). Structural disorganization observed in old hearts may be attributed to the excessive deposition of connective tissue indicating a pathogenic remodeling process.

4. Discussion

Our study demonstrates a NLOM based label-free imaging approach for a comprehensive assessment of age-related structural differences in the cardiac tissue obtained from non-human primates (NHPs). By successfully segregating the collagen originated SHG as the backscattered signal from myosin emitted SHG, a reliable quantification of connective tissue content was performed in neonatal (<4 weeks), young adult (1-4 years) and old (>10 years) marmosets. Additionally, the total scattering tissue volume (myosin + collagen) which was detected as forward SHG signal was determined in 3D for all groups. Myosin emitted SHG was quantified in overview as well as in zoomed-in images to provide vital cues for evaluating age-related structural differences. Our results demonstrate for the first time, significant differences in total scattering tissue volume, myofibril spacing, alignment, curvature, and angular distribution in hearts of marmosets of different age groups using a label-free NLOM imaging approach.

Imaging intrinsic signals in form of TPEF and SHG provided reliable high-resolution visualization of various structures in marmoset hearts at the cellular and subcellular levels, such as cardiomyocytes (CMs), collagen, elastin, nuclei and myosin. In our previous study, the collagen emitted SHG signal was morphologically identified as fibrous structure and myosin by its typical striated pattern [27]. SHG is an anisotropic process that mainly propagates in the direction of the incident light with a minor fraction of backscattered signal. Compared to myosin, collagen is a very strong SH generator at excitation wavelengths above 800 nm [24,30]

Biomedical Optics EXPRESS

and our results demonstrate that it provides a suitable quantitative signal in epi-direction as well. Myosin, on the other hand, requires a higher threshold of excitation energy to be detected in the epi-direction. Harnessing these differences, we successfully developed a simple strategy to detect collagen emitted SHG in backward direction with a negligible signal from myosin. However, one limitation involving this approach is that the horizontally oriented collagen fibers scatter bidirectionally while the vertically oriented collagen fibers scatter mostly in the forward direction [24,31]. Since relatively thin tissue slices (50 or 100 µm) were used, this difference was minimized [32]. Importantly, the quantification of collagen for all age groups was also performed in epi-direction only. Nonetheless, the detection of collagen fibers with variable orientation in thicker samples could be optimized by altering the polarization of excitation light and/or by adjusting the sample orientation, as has been previously performed [24,32].

Myosin emitted only a weak SHG signal in epi-direction as demonstrated by our results and is highly influenced by the orientation of the myofibrils and semicrystalline order of A-bands [27,33]. While our image acquisition settings resulted in optimal SH signal intensity from myosin at the forward detector, they also caused minimal signal saturation from collagen SHG. This can be attributed to the structural assembly of both harmonophores as collagen fibers associate into bundles and generally have a greater diameter than myosin fibers [27,30].

By using this label-free imaging approach, age-related structural differences were found in common marmoset monkeys divided into three groups neonatal, young adult and old. This selection of age groups matches with the previously reported aging profile of common marmoset monkeys kept in captivity for both male and female [28]. Volumetric analysis showed a significant increase in collagen at the myocardium with aging. The interplay of various signaling pathways contributes to the maturation, as well as pathological deposition of ECM [11]. Recently, it has been established that fibroblasts are a key constituent in the microenvironment promoting cardiac maturation [34]. The low volume of collagen detected in neonatal hearts is because the fibroblasts increase postnatally until adulthood [34]. Under healthy conditions (i.e., the adult hearts) cardiac fibroblasts regulate ECM content and provide a scaffold for CMs [34]. During aging the fibroblasts undergo fibroblast-to-myofibroblast transition which produces profibrotic factors, driving fibrosis progression. In aged hearts, the myofibroblasts mediated attenuation of the matrix-degrading pathways [11,13,35] can contribute to the excessive collagen volume that was observed in the old hearts as shown by the 3D analysis. Development of age-related fibrosis has been reported previously in marmosets with a minor effect on cardiac functional efficiency [14]. Our approach for the first time provides reliable label-free volumetric quantification of age-related collagen remodeling in NHPs. The collagen volume in old animals was found to be significantly increased as compared to neonatal and adult marmosets.

Our results also revealed an increase in the total scattering tissue volume (myosin + collagen) which was detected as forward SHG with aging in marmosets. These findings support the notion that even after cell-cycle withdrawal, a postnatal heart continues to gain volume by a proportional increase in CM mass and myofibril expansion until early adulthood through a process called physiological or maturational hypertrophy [5,36,37]. This tissue growth and maturation process reduces the overall spacing between myofibrils by early adulthood and results in a significant increase in tissue volume. Conversely, the aged hearts involve apoptosis induced reduction in the number of CM and an overall lower LV mass [14,38,40]. Our 3D analysis, however, showed a significantly higher total scattering tissue volume in the old marmoset hearts at the ROIs as compared to the neonatal and adult hearts indicating a progressive increase in LV mass at pathological sites. We postulate that the CM loss is compensated by the age-related pathophysiological CM hypertrophy and excessive collagen deposition in the interstitial space potentially caused by arterial stiffening and increased hemodynamic load [39–42].

In the neonatal hearts, lower scattering tissue volume coincides with the higher degree of spacing reflected by increased myofibril length. The myofibril curvature, alignment, and angle

Biomedical Optics EXPRESS

are also significantly different from the adult and old marmoset hearts. It was further established that neonatal cardiac tissue lacked fully developed ICDs at this developmental stage in marmosets as these could not be visualized in the SHG images. This indicates that ICD associated cell adhesion structures including fascia adherens, desmosomes, and gap junctions are also not fully expressed in neonates contributing to the structural disassembly. Moreover, it is known that CM integration requires attachment to ECM via focal adhesion structures called costameres which are also not developed in the neonatal hearts [43]. Besides tissue integration, the ICDs and costameres also contribute to CM maturation by harboring vinculin-based actomyosin assembly that is required for sarcomere expansion [5,43]. By early adulthood, the targeted localization of ICD and costameric components to the CM termini does indeed occur, which was evident by the clear banding and improved alignment of myofibrils as observed in young adult marmoset hearts.

In the old marmoset hearts, the disorganization of the myocardium indicates pathological remodeling of the cardiac tissue at several heterogeneously distributed regions of interest. Our results highlight significant age-related alterations in the overall alignment, curvature and angular distribution of the hypercontracted myofibrils. We postulate that the presence of high ECM content and distorted myofibrils are the main contributors to the structural disassembly in the old hearts. Several studies have reported cardiac hypercontractility caused by hypertrophic cardiomyopathies [44]. Our previous work also showed hypertrophy induced myofibril undulation and hypercontractility using SHG imaging in a cardiac pressure-overload mouse model [27]. In addition to hypertrophy, age-related hypercontractility is linked to cardiac stiffness and abnormalities in cardiac ECC due to Ca^{2+} overload. A recent study reported the expression of the Transient Receptor Potential Vanilloid-4 (TRPV4) – a non-selective cation channel – in aged mouse hearts causing an additional sarcolemmal Ca^{2+} influx pathway [45]. This consequently contributes to excessive intracellular Ca^{2+} accumulation provoking cardiac hypercontractility. Our data strongly indicate loss of structural integrity in aged hearts and provide a potential therapeutic target for maintaining cardiac function in elderly patients.

TPEF and histological assessment validated the basic differences in the myocardium in all three-age groups. The high nuclear to cytoplasm ratio in the neonatal hearts declines as the CMs mature in adult mammalian hearts, as observed in TPEF and histological images, which mainly occurs via DNA synthesis without nuclear division to make polyploid nuclei [46,47]. Morphologically, it was also evident that the nuclei in mature CM are larger than neonatal ones which can be attributed to the higher DNA content in adult hearts.

In summary, this study shows that the transition of the cardiac tissue from an immature state in neonatal marmoset heart to an adult mature one involves an increase in size and gain in structural organization, volume, and binding of the myofibrils via the formation of fully developed ICDs and ECM maturation. In old marmoset hearts, pathological remodeling of cardiac tissue results in loss of structural organization due to excessive collagen deposition and hypercontractile state of myofibrils. Further, taking into account the cardiovascular similarities shared between marmosets and humans, this imaging approach can be applied as a powerful tool for analysing human cardiac tissue in detail. These findings also highlight the unrivalled potential of NLOM label-free imaging that can be further applied for monitoring the effects of therapeutic approaches for cardiac regeneration and repair on the structural level. They also provide essential foundations for intravital imaging using NLOM of cardiac developmental and pathological remodeling. Advanced understanding of cardiac structural maturation and age-related remodeling can elucidate biophysical and biochemical cues causing abnormal cardiac maturation and aging.

Funding. Niedersächsisches Ministerium für Wissenschaft und Kultur; Deutsche Forschungsgemeinschaft.

Acknowledgments. We thank Bärbel Heidrich and Regine Kurse for assistance in sample preparation, and Bettina Jeep and Sabine Wolfgramm for providing technical assistance for histology. We would also like to thank Miso Mitkovski and Heiko Röhse from the MPI-EM light microscopy facility (LMF) for assistance with NLOM microscope.

Biomedical Optics EXPRESS

This work was supported by the "Multiscale Bioimaging" (MBExC) Cluster of Excellence EXC 2067/1- 39072994 (DFG). AK was supported by a seed grant of the "Physics-to-Medicine Initiative Göttingen (MWK)."

Disclosures. The authors declare that they have no competing interests.

Data availability. Data underlying the results presented in this paper are not publicly available but may be obtained from the authors upon request.

Supplemental document. See Supplement 1 for supporting content.

References

1. G. Maroli and T. Braun, "The long and winding road of cardiomyocyte maturation," Cardiovasc. Res. **117**(3), 712–726 (2021).
2. M.-T. Zhao, S. Ye, J. Su, and V. Garg, "Cardiomyocyte proliferation and maturation: two sides of the same coin for heart regeneration," Front. Cell Dev. Biol. **8**, 594226 (2020).
3. N. Velayutham, E. J. Agnew, and K. E. Yutzey, "Postnatal cardiac development and regenerative potential in large mammals," Pediatr. Cardiol. **40**(7), 1345–1358 (2019).
4. M. Günthel, P. Barnett, and V. M. Christoffels, "Development, proliferation, and growth of the mammalian heart," Mol Ther **26**(7), 1599–1609 (2018).
5. G. Yuxuan and P. William T, "Cardiomyocyte maturation," Circ. Res. **126**(8), 1086–1106 (2020).
6. M. Ponnusamy, P.-F. Li, and K. Wang, "Understanding cardiomyocyte proliferation: an insight into cell cycle activity," Cell. Mol. Life Sci. **74**(6), 1019–1034 (2017).
7. M. Mollova, K. Bersell, S. Walsh, J. Savla, L. T. Das, S.-Y. Park, L. E. Silberstein, C. G. dos Remedios, D. Graham, S. Colan, and B. Kühn, "Cardiomyocyte proliferation contributes to heart growth in young humans," Proc. Natl. Acad. Sci. U. S. A. **110**(4), 1446–1451 (2013).
8. O. Bergmann, R. D. Bhardwaj, S. Bernard, S. Zdunek, F. Barnabé-Heider, S. Walsh, J. Zupicich, K. Alkass, B. A. Buchholz, H. Druid, S. Jovinge, and J. Frisén, "Evidence for cardiomyocyte renewal in humans," Science **324**(5923), 98–102 (2009).
9. V. Obas and R. S. Vasan, "The aging heart," Clin. Sci. **132**(13), 1367–1382 (2018).
10. B. A. Borlaug, "Evaluation and management of heart failure with preserved ejection fraction," Nat. Rev. Cardiol. **17**(9), 559–573 (2020).
11. C. A. Meschiari, O. K. Ero, H. Pan, T. Finkel, and M. L. Lindsey, "The impact of aging on cardiac extracellular matrix," GeroScience **39**(1), 7–18 (2017).
12. J. A. C. Lima, "The aging human heart," Circ Cardiovasc Imaging **10**(1), e005899 (2017).
13. A. Biernacka and N. G. Frangogiannis, "Aging and cardiac fibrosis," Aging Dis **2**(2), 158–173 (2011).
14. A. Moussavi, M. Mietsch, C. Drummer, R. Behr, J. Mylius, and S. Boretius, "Cardiac MRI in common marmosets revealing age-dependency of cardiac function," Sci Rep **10**(1), 10221 (2020).
15. N. G. Frangogiannis, "Cardiac fibrosis: cell biological mechanisms, molecular pathways and therapeutic opportunities," Mol Aspects Med **65**, 70–99 (2019).
16. W. Chen and N. G. Frangogiannis, "The role of inflammatory and fibrogenic pathways in heart failure associated with aging," Heart Fail Rev **15**(5), 415–422 (2010).
17. H. A. Feridooni, K. M. Dibb, and S. E. Howlett, "How cardiomyocyte excitation, calcium release and contraction become altered with age," J. Mol. Cell. Cardiol. **83**, 62–72 (2015).
18. J. A. Mattison and K. L. Vaughan, "An overview of nonhuman primates in aging research," Exp Gerontol **94**, 41–45 (2017).
19. T. Kohl, V. Westphal, S. W. Hell, and S. E. Lehnart, "Superresolution microscopy in heart—cardiac nanoscopy," J. Mol. Cell. Cardiol. **58**, 13–21 (2013).
20. B. R. Long, D. C. Robinson, and H. Zhong, "Subdiffractive microscopy: techniques, applications, and challenges," WIREs Syst Biol Med **6**(2), 151–168 (2014).
21. L. Wang, B. Chen, W. Yan, Z. Yang, X. Peng, D. Lin, X. Weng, T. Ye, and J. Qu, "Resolution improvement in STED super-resolution microscopy at low power using a phasor plot approach," Nanoscale **10**(34), 16252–16260 (2018).
22. J. Liu, "Two-photon microscopy in pre-clinical and clinical cancer research," Front. Optoelectron. **8**(2), 141–151 (2015).
23. V. Parodi, E. Jacchetti, R. Osellame, G. Cerullo, D. Polli, and M. T. Raimondi, "Nonlinear optical microscopy: from fundamentals to applications in live bioimaging," Front. Bioeng. Biotechnol. **8**, 1174 (2020).
24. P. Friedl, K. Wolf, G. Harms, and U. H. von Andrian, "Biological second and third harmonic generation microscopy," Curr. Protoc. Cell Biol. **34**(1), 4.15.1 (2007).
25. S. W. Perry, R. M. Burke, and E. B. Brown, "Two-photon and second harmonic microscopy in clinical and translational cancer research," Ann Biomed Eng **40**(2), 277–291 (2012).
26. B. Weigelin, G.-J. Bakker, and P. Friedl, "Third harmonic generation microscopy of cells and tissue organization," J Cell Sci **129**(2), 245–255 (2016).
27. J.-D. Nicolas, A. Khan, A. Markus, B. A. Mohamed, K. Toischer, F. Alves, and T. Salditt, "X-ray diffraction and second harmonic imaging reveal new insights into structural alterations caused by pressure-overload in murine hearts," Sci. Rep. **10**(1), 19317 (2020).

Biomedical Optics EXPRESS

28. D. H. Abbott, D. K. Barnett, R. J. Colman, M. E. Yamamoto, and N. J. Schultz-Darken, "Aspects of common marmoset basic biology and life history important for biomedical research," Comp. Med. **53**(4), 339–350 (2003).
29. E. Wershof, D. Park, D. J. Barry, R. P. Jenkins, A. Rullan, A. Wilkins, K. Schlegelmilch, I. Roxanis, K. I. Anderson, P. A. Bates, and E. Sahai, "A FIJI macro for quantifying pattern in extracellular matrix," Life Sci. Alliance **4**(3), e202000880 (2021).
30. N. H. Green, R. M. Delaine-Smith, H. J. Askew, R. Byers, G. C. Reilly, and S. J. Matcher, "A new mode of contrast in biological second harmonic generation microscopy," Sci. Rep. **7**(1), 13331 (2017).
31. W. R. Zipfel, R. M. Williams, R. Christiet, A. Y. Nikitin, B. T. Hyman, and W. W. Webb, "Live tissue intrinsic emission microscopy using multiphoton-excited native fluorescence and second harmonic generation," Proc. Natl. Acad. Sci. U. S. A. **100**(12), 7075–7080 (2003).
32. X. Chen, O. Nadiarynkh, S. Plotnikov, and P. J. Campagnola, "Second harmonic generation microscopy for quantitative analysis of collagen fibrillar structure," Nat Protoc **7**(4), 654–669 (2012).
33. C. Greenhalgh, N. Prent, C. Green, R. Cisek, A. Major, B. Stewart, and V. Barzda, "Influence of semicrystalline order on the second-harmonic generation efficiency in the anisotropic bands of myocytes," Appl. Opt. **46**(10), 1852 (2007).
34. H. Caitlin, G. Katja, D. Chris, and P. Davor, "Complex relationship between cardiac fibroblasts and cardiomyocytes in health and disease," J. Am. Heart Assoc. **10**(5), e019338 (2021).
35. M. D. Tallquist, "Cardiac fibroblast diversity," Annu. Rev. Physiol. **82**(1), 63–78 (2020).
36. Y. Guo, B. D. Jardin, P. Zhou, I. Sethi, B. N. Akerberg, C. N. Toepfer, Y. Ai, Y. Li, Q. Ma, S. Guatimosim, Y. Hu, G. Varuzhanyan, N. J. VanDusen, D. Zhang, D. C. Chan, G.-C. Yuan, C. E. Seidman, J. G. Seidman, and W. T. Pu, "Hierarchical and stage-specific regulation of murine cardiomyocyte maturation by serum response factor," Nat. Commun. **9**(1), 3837 (2018).
37. F. X. Galdos, Y. Guo, S. L. Paige, N. J. VanDusen, S. M. Wu, and W. T. Pu, "Circulation Research Compendium–cardiac regeneration: lessons from development," Circ. Res. **120**(6), 941–959 (2017).
38. G. Olivetti, M. Melissari, J. M. Capasso, and P. Anversa, "Cardiomyopathy of the aging human heart. Myocyte loss and reactive cellular hypertrophy," Circ. Res. **68**(6), 1560–1568 (1991).
39. E. G. Lakatta, "Age-associated cardiovascular changes in health: impact on cardiovascular disease in older persons," Heart Fail Rev **7**(1), 29–49 (2002).
40. L. Haobo, H. Margaret H., R. James, T. Lena E., R. Jason D., and R. Anthony, "Targeting Age-Related Pathways in Heart Failure," Circ. Res. **126**(4), 533–551 (2020).
41. M. A. Horn and A. W. Trafford, "Aging and the cardiac collagen matrix: novel mediators of fibrotic remodelling," J. Mol. Cell. Cardiol. **93**, 175–185 (2016).
42. N. S. V. Singam, C. Fine, and J. L. Fleg, "Cardiac changes associated with vascular aging," Clin. Cardiol. **43**(2), 92–98 (2020).
43. A. M. Samarel, "Costameres, focal adhesions, and cardiomyocyte mechanotransduction," American Journal of Physiology-Heart and Circulatory Physiology **289**(6), H2291–H2301 (2005).
44. C. V. Tuohy, S. Kaul, H. K. Song, B. Nazer, and S. B. Heitner, "Hypertrophic cardiomyopathy: the future of treatment," Eur J Heart Fail **22**(2), 228–240 (2020).
45. A. B. Veteto, D. Peana, M. D. Lambert, K. S. McDonald, and T. L. Domeier, "Transient receptor potential vanilloid-4 contributes to stretch-induced hypercontractility and time-dependent dysfunction in the aged heart," Cardiovasc. Res. **116**(11), 1887–1896 (2020).
46. S. P. Bishop, Y. Zhou, Y. Nakada, and J. Zhang, "Changes in cardiomyocyte cell cycle and hypertrophic growth during fetal to adult in mammals," JAHA **10**(2), e017839 (2021).
47. E. Karbassi, A. Fenix, S. Marchiano, N. Muraoka, K. Nakamura, X. Yang, and C. E. Murry, "Cardiomyocyte maturation: advances in knowledge and implications for regenerative medicine," Nat Rev Cardiol **17**(6), 341–359 (2020).